



# Gone in a Picosecond

*Himanshu Aggrawal, Peiyu Chen, M. Mahdi Assefzadeh, Babak Jamali, and Aydin Babakhani*

**T**he technology for generating and detecting electromagnetic waves has evolved significantly over the last 120 years. In the early 1890s, Guglielmo Marconi used a spark-gap transmitter to build a wireless telegraphy system. In his design, he charged a capacitor to a high dc voltage and connected it to a parallel combination of an inductor, a second capacitor, and an antenna through an air gap. In this configuration, when the dc voltage of the first capacitor reaches the breakdown voltage of the gap, the air in the gap ionizes and reduces the resistance across the gap. This results in a large step voltage applied to the parallel combination of the inductor, second capacitor, and the antenna and converts the dc energy stored in the first capacitor to a damped oscillation at a low megahertz range that is radiated from the antenna. Marconi's design used the spark gap as a fast high-voltage switch. The technology for generating electromagnetic waves then evolved further with the invention of vacuum tubes in the mid-1920s. Vacuum tubes enabled oscillatory signals to

be amplified in the megahertz range and provided enough bandwidth for transferring audio signals.

At the start of World War II, the radar application of electromagnetic waves received significant attention. Major resources were allocated for developing pulsed radars in the microwave range to locate war planes by measuring the round-trip travel time of the electromagnetic pulses. In addition, the time-domain signature of the reflected pulses was analyzed to identify different types of aircraft. In this application, shorter pulses are preferred because the reflection of a short pulse from different parts of an aircraft arrives in different times, making it easier to identify the object.

## **Electromagnetic Wave Technology Today**

During the second half of the 20th century, spurred by the birth of transistors and integrated circuits, the cost of producing electromagnetic signals in the gigahertz range was greatly reduced. This resulted in the birth of cellular networks for consumer applications. Due to the non-line-of-sight (NLOS) nature of cellular links and the high-frequency dependency of NLOS links,

---

*Himanshu Aggrawal (himanshu@rice.edu), Peiyu Chen (peiyu.chen@rice.edu), M. Mahdi Assefzadeh (mahdi@rice.edu), Babak Jamali (babak.jamali@rice.edu), and Aydin Babakhani (aydin.babakhani@rice.edu) are with Rice University, Houston, Texas, United States.*

the communication channels were separated in the frequency domain to minimize interference among multiple users. In a rich-scattering NLOS channel, where the bandwidth of a single user is much smaller than the aggregate bandwidth of the entire network, it is easier to separate the users in the frequency domain. This is because a user can filter out the signals generated by other users in the frequency domain and does not need to receive any feedback from other users to demodulate its own signal.

Over the past decade, there has been a significant shift toward millimeter (mm)-wave and terahertz frequencies due to advances in source/detector technologies and the rapidly rising demand for wireless data [1]–[5]. In addition to high-speed wireless communication, other applications enabled by mm-wave and terahertz frequencies include high-resolution three-dimensional (3-D) imaging radars for security monitoring and autonomous driving, miniaturized radars for gesture detection and touchless smartphones, spectrometers for explosive detection and gas sensing, precision time/frequency transfer, and wireless synchronization of widely spaced arrays. In addition, secure line-of-sight (LOS) communication (directional modulation) is enabled by joint spatial coding through widely spaced transmitters. Figure 1 illustrates some of these applications and the efforts made over the past decade to push the required technologies to higher frequencies.

Electromagnetic waves in the mm-wave and terahertz frequencies and their source/detector technologies have several key differences versus their RF and microwave counterparts. First, mm-wave and terahertz waves experience a high loss in NLOS environments. In these frequencies, the transmitters produce a highly directive laser-like beam that travels in a LOS path to a receiver (or to an object) but suffers a high loss in a NLOS channel. Second, due to the small size of the antennas and low power levels, a large number of coherent transmit elements is required to boost the power and increase the effective aperture size while enabling broadband electronic beamsteering. Third, the fundamental oscillators in the mm-wave and terahertz ranges lack the required frequency stability and suffer from high phase noise due to the low gain of the transistors in the mm-wave and terahertz ranges. To lock these oscillators to a stable reference signal at a low frequency, a power-consuming phase lock loop equipped with many divider stages is required.

To address these issues and support a large data rate (several hundred gigabits per second) over a practical LOS distance (e.g., 100 m), one needs to build a large array of tightly synchronized transmitters and receivers that can produce signals with instantaneous bandwidth exceeding 100 GHz. One approach to address this challenge is to produce pulses with durations of a few picoseconds and perform amplitude

## **Over the past decade, there has been a significant shift toward millimeter-wave and terahertz frequencies due to advances in source/detector technologies and the rapidly rising demand for wireless data.**

modulation to achieve the required data rate. In this approach, beamsteering can be accomplished merely by introducing time delay in the transmitted pulses.

Currently, the most common technique for producing and detecting broadband pulses is to use a femtosecond laser. However, laser-based systems are bulky, have low repetition rates, and require a sensitive optical alignment to operate. To mitigate this issue, one needs to design a fully electronic, laser-free method for producing and detecting picosecond pulses. Toward this goal, in this article we report multiple picosecond source/detector technologies based on laser-free, fully electronic integrated circuits. The reported picosecond source technologies can produce a frequency comb exceeding 1 THz, which is five times higher than the  $f_T$  of the transistor used in the circuit [6]. The produced terahertz tones have a line width of better than 2 Hz, which can be used for precision time/frequency transfer and localization [6]. The generated picosecond pulses have a timing jitter of better than 200 fs, enabling depth sensing accurate to 60  $\mu\text{m}$  or better. The detectors equipped with on-chip antennas are designed to capture the picosecond pulses and, by extracting their amplitude and repetition frequency, enable wireless synchronization of a large mm-wave array [7].

### **Picosecond Sources**

#### ***Laser-Based Techniques***

Picosecond pulses are traditionally generated with a femtosecond laser and a photo-conductive antenna (PCA). The procedure requires biasing two electrodes of a PCA with a dc voltage, thereby generating an electric field on a semiconducting material. Although no current flows in the absence of optical illumination, an ultrashort (~100 fs) optical pulse generates electrons and holes, which produce a current due to the electric field. Because of the small transition region (a few microns) and the short transport time, this technique can generate subpicosecond pulses. As illustrated in Figure 2, laser excitation of a PCA generates broadband picosecond radiation with frequencies reaching above 1 THz [35].

Broadband radiation can be detected by a similar method. In this case, a femtosecond laser pulse is used to sample an incoming terahertz beam at the center of a PCA antenna. The spectroscopy based on this method of applying a femtosecond laser with source/detector

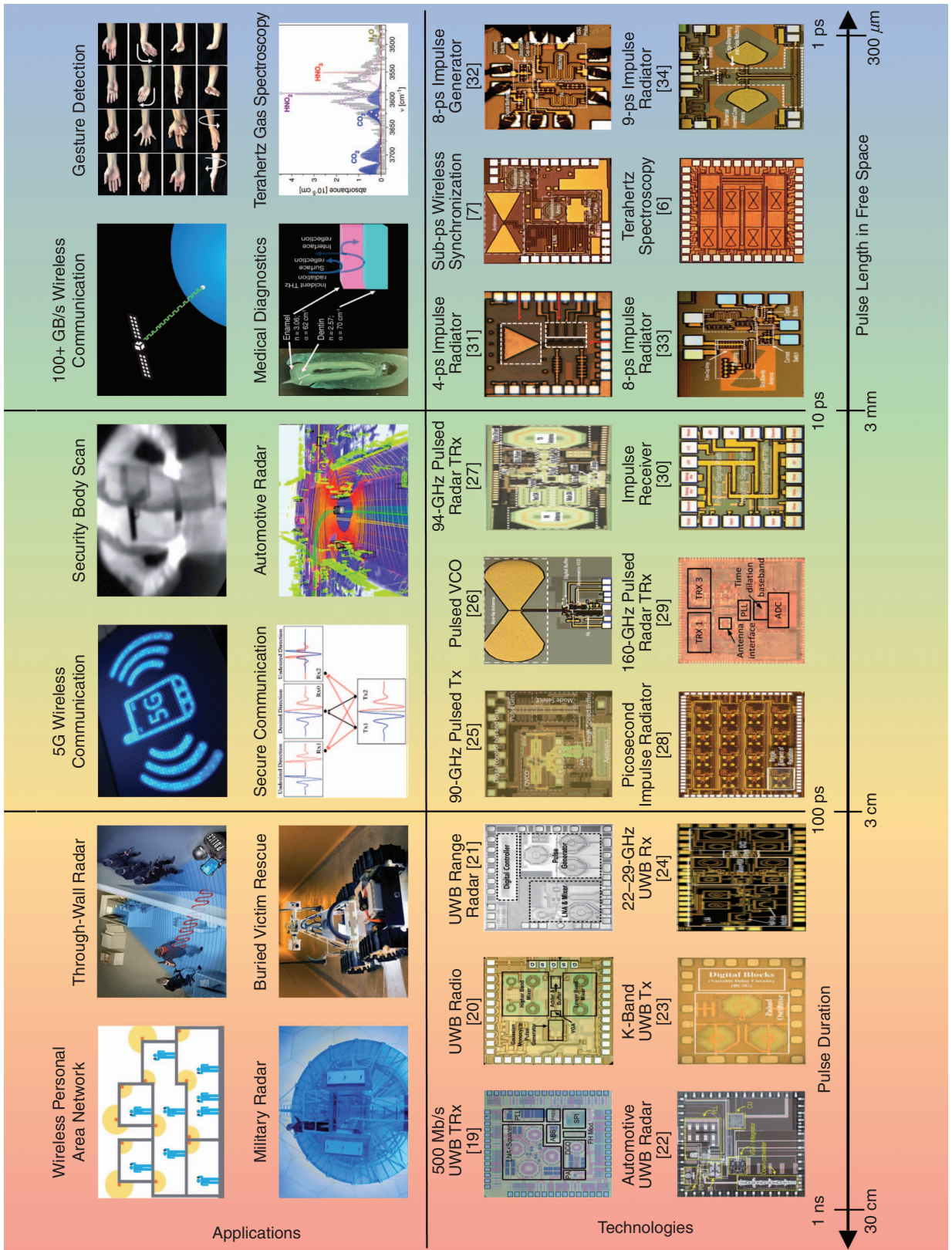


**Figure 1.** Examples of millimeter-wave and terahertz technologies and their applications. 5G: fifth-generation; UWB: ultrawide-band; Tx: transmitter; Rx: receiver; TRx: transceiver.

PCAs is referred to as *terahertz time-domain spectroscopy (THz-TDS)*. A conventional THz-TDS system has several drawbacks. It requires a bulky and expensive

laser. It also needs a time-consuming optical alignment. The laser has a low repetition rate ( $< 100$  MHz), which translates to a low average radiated power

( $\sim 1 \mu W$ ). Conventional THz-TDS systems use a single source and a single detector and provide no beam-steering capability; to generate images, one must move the object mechanically. Capturing the entire pulse requires a mechanical delay line to vary the time of the sampling. The slow speed of the mechanical delay line translates into a slow acquisition speed.

An alternative solution to the mechanical delay line is a two-laser system with a frequency offset. A slight difference in the repetition rate of the two lasers is used to shift the sampling window. This setup removes the bulky mechanical line, but at the expense of an extra laser. To overcome these disadvantages, a laser-free, fully electronic approach for generating and detecting picosecond pulses is required.

### Laser-Free, Fully Electronic Terahertz Sources

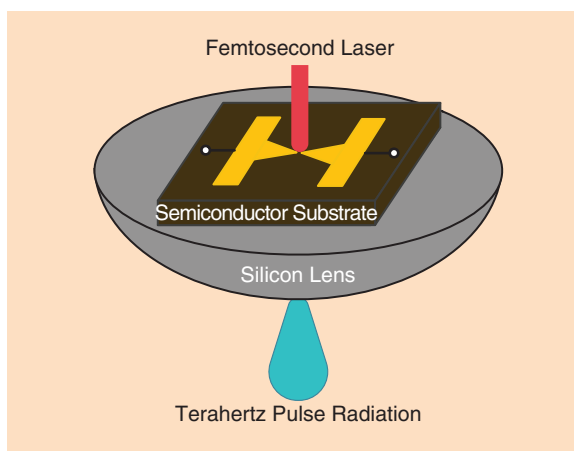
To conduct terahertz spectroscopy and generate high-resolution 3-D radar images, ultrashort pulses with broad frequency spectra are required. Several recent publications have reported silicon-based broadband signal radiation with pulsewidth shorter than 50 ps. The following sections review some of these techniques.

### Oscillator-Based Continuous Wave Designs

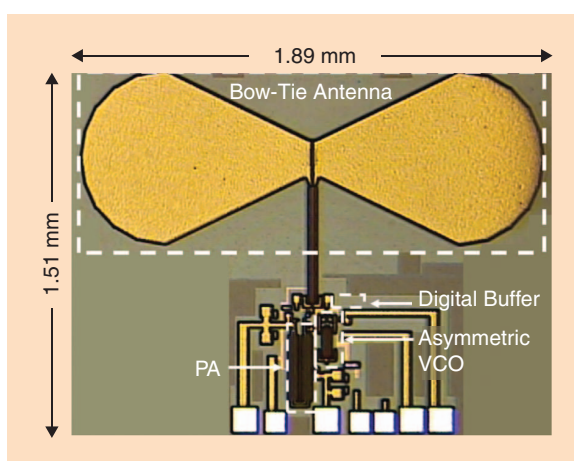
Impulses can be generated by switching voltage-controlled oscillators (VCOs). However, simply switching a conventional VCO that has a symmetric topology will induce phase-ambiguity problems. To mitigate this issue, an asymmetric cross-coupled VCO is proposed in [26]. The asymmetric VCO can produce impulses with a deterministic starting phase that is locked to an input trigger. In an asymmetric cross-coupled pair, the size of one transistor is larger than the other, which causes a deterministic initial condition. A prototype chip is implemented in a 130-nm silicon germanium (SiGe) bipolar junction complementary metal-oxide-semiconductor (BiCMOS) process technology that uses a 30-GHz asymmetric VCO and an on-chip antenna (Figure 3). The chip can radiate impulses with a full-width-at-half-maximum (FWHM) parameter of 60 ps. The radiated impulses have a root mean square (RMS) jitter of 178 fs. Figure 4 demonstrates spatial-impulse combining that uses two of these chips. The measured combined impulse waveform is almost identical to the algebraic summation of the two impulses radiated by the two individual impulse radiators.

### Direct Digital-to-Impulse

An 8-ps impulse radiator reported in [33] is based on an oscillatorless direct digital-to-impulse (D2I) topology. In this design, magnetic energy is stored in a broadband, phase-linear antenna carrying a dc current. A fast current switch abruptly releases the stored magnetic energy, transferring the rising/falling edge of a digital input trigger into an impulse radiation.



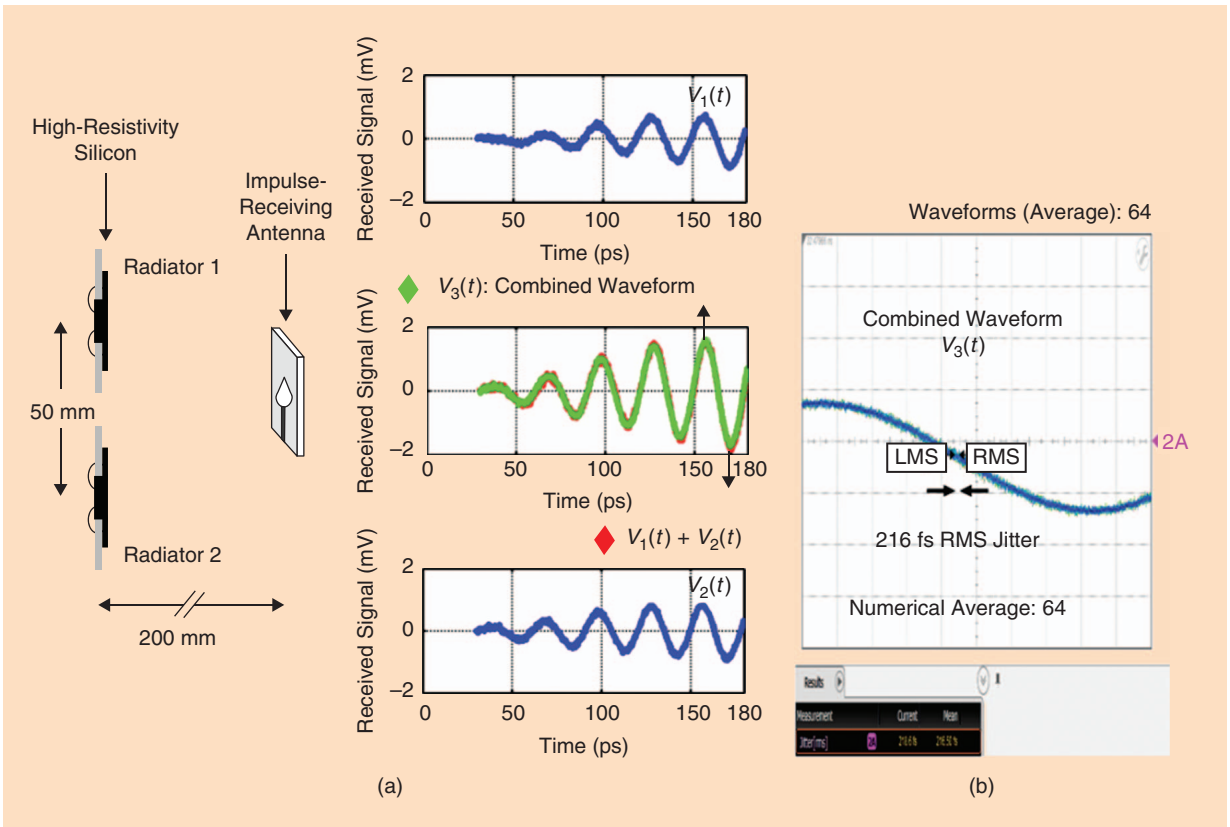
**Figure 2.** The terahertz pulse radiation with a femtosecond laser and a PCA.



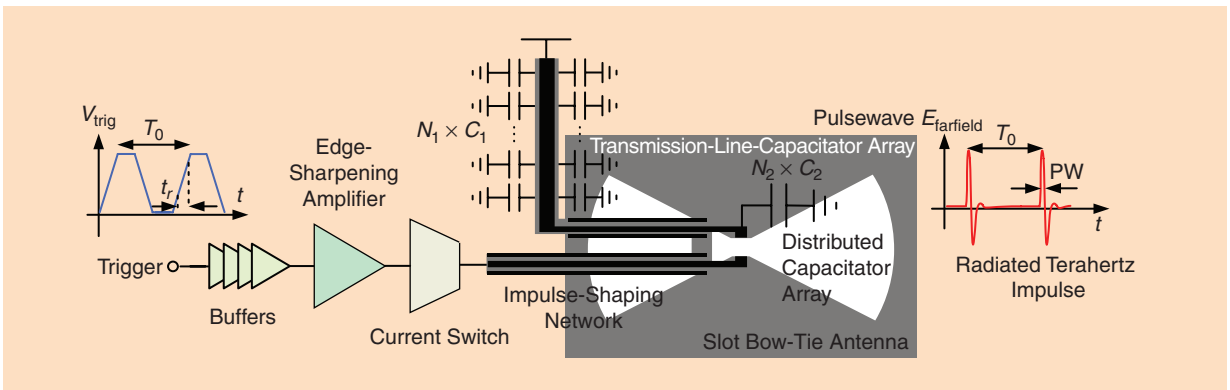
**Figure 3.** A micrograph of a chip with an oscillator-based impulse generator [26]. PA: power amplifier.

Figure 5 shows the block diagram and schematic of the 8-ps D2I impulse radiator. In this circuit, a digital trigger signal with a rise time of 120 ps arrives at the input of the chip. A series of digital buffers reduces the rise time of the signal to 30 ps and sends it to a power amplifier for further amplification. A broadband slot bow-tie antenna designed to radiate ultrashort impulses is connected to a bipolar switch. When the switch is in its ON position, a dc current energizes the antenna; when the power amplifier turns the switch to OFF, the current stored in the antenna radiates ultrashort impulses that are coherent with the digital trigger. A transmission-line-based pulse-matching network maximizes the energy of each impulse while minimizing its duration. Figure 6 reports the 8-ps pulses radiated by the chip, and Figure 7 shows a micrograph of the chip, which occupies an area of  $0.55 \text{ mm} \times 0.85 \text{ mm}$  fabricated in a 130-nm SiGe BiCMOS process. The chip radiates impulses with peak effective isotropic radiated power (EIRP) of 20 mW.

The D2I architecture offers several key advantages over oscillator-based continuous wave designs.



**Figure 4.** The coherent spatial pulse combining of two widely spaced radiators [26]. LMS: least mean square.



**Figure 5.** The schematic of the direct D2I radiator [33].

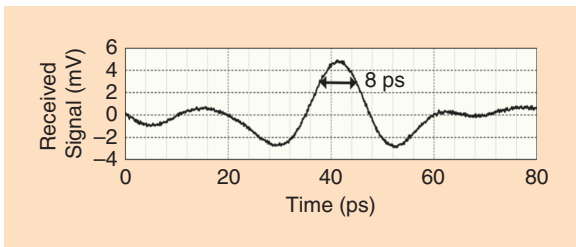


**Figure 6.** The time-domain waveform of an 8-ps radiated pulse [33].

- Because the starting time of the impulse synchronizes with the rise time of the input trigger signal, the starting time can be controlled by delaying the trigger signal. This unique characteristic used in an array configuration delivers a major advantage, making it possible to achieve broadband beamsteering by delaying the trigger signal. In this design, all frequency components of the pulse experience exactly the same time delay.
- When a stable low-frequency clock generates the trigger signal periodically, the radiated signal forms an impulse train with a repetition frequency that equals the clock frequency, resulting in a frequency-comb spectrum suitable for broadband terahertz spectroscopy.
- The broadband pulse covers a wide range of frequencies, making it an ideal candidate for terahertz spectroscopy and 3-D imaging radar.

To increase the radiated power and gain beamsteering capability, an array of impulse radiators is used. An aperture created by a coherent impulse radiator array with  $N$ -elements can improve the received power by a factor of  $N^2$ . Moreover, the point where all the pulses combine coherently can be changed by merely varying the delays on each radiator. As shown in Figure 8, a  $4 \times 4$  array was fabricated where the impulses from each element are coherently combined in air [28]. In this  $4 \times 4$  array, a single trigger signal is fed to the chip and routed to 16 radiators in an H-tree scheme. In addition, a digitally programmable delay block is used at each element to align the radiated pulses in the space with accuracy of 200 fs. This chip produces 14-ps pulses with peak EIRP of 17 dBm. The chip was implemented in a 65-nm bulk CMOS process technology and occupies an area of  $3.3 \text{ mm} \times 2.0 \text{ mm}$ .

To reduce the duration of the radiated pulses to 4 ps, the technique of nonlinear Q-switching impedance (NLQSI) is reported in [31]. In this method, the NLQSI element passes the positive pulse to the antenna, but, to avoid ringings and reduce the pulse duration, it changes the quality factor of the tank when the pulse becomes negative. This method enables generation and radiation of impulses with a FWHM of 4 ps. Figure 9 shows the time-domain pulses radiated by the chip measured using a novel laser-sampling method [31]. The impulse radiator radiates 4-ps pulses with a signal-to-noise ratio  $> 1$  bandwidth of more than 160 GHz. This chip allows amplitude reconfiguration capability using a four-way on-chip inductive impulse combining scheme. This chip is fabricated in a 130-nm SiGe BiCMOS process and occupies an area of  $1 \text{ mm}^2$ . A micrograph of the chip is shown in Figure 10.

To further increase the power and reduce the duration of the radiated pulses, a  $4 \times 2$  SiGe BiCMOS D2I chip is reported in [6]. The chip is equipped with a programmable delay block at each element and radiates pulses with FWHM of 5.4 ps and peak EIRP of 1 W. Figure 11 shows a micrograph of the chip. The chip is fabricated in a 90-nm SiGe BiCMOS technology and occupies an area of  $1.6 \text{ mm} \times 1.5 \text{ mm}$ .

## Picosecond Detectors

### High-Speed Sampling with Optical Methods

Currently, the most common technique to sample a picosecond signal is via photoconductive detection

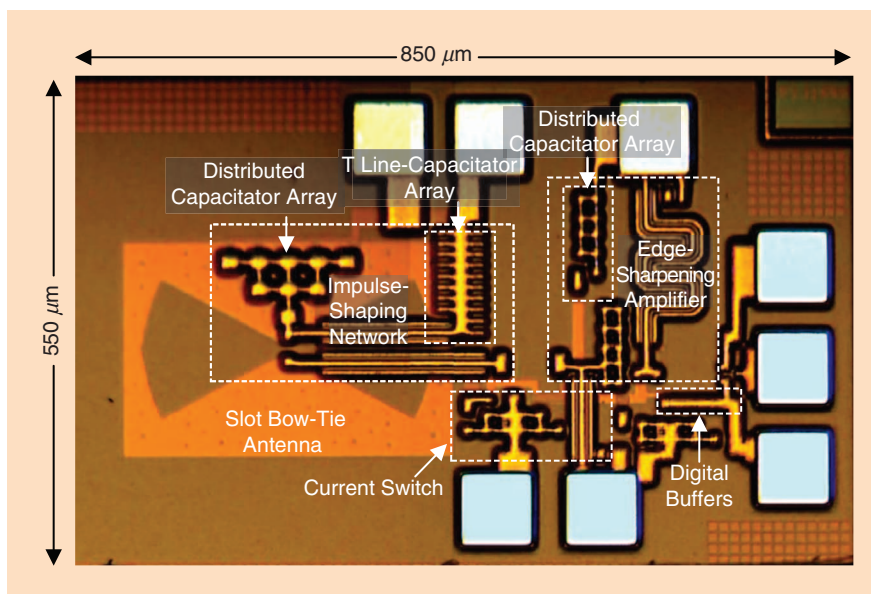


Figure 7. A micrograph of the chip for the D2I radiator [33].

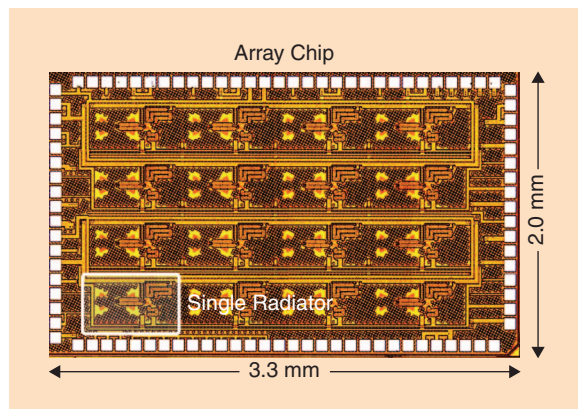


Figure 8. A chip micrograph of the D2I radiator array [28].

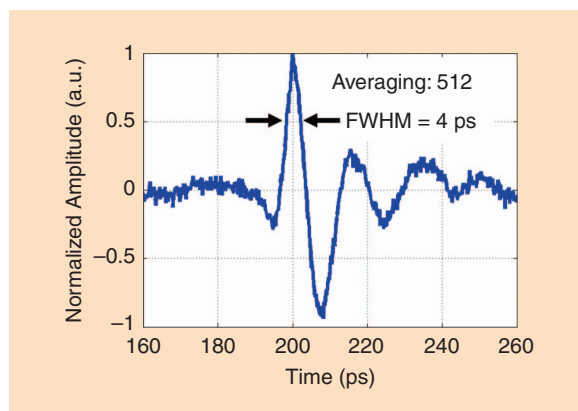


Figure 9. The measured time-domain waveform of a 4-ps impulse radiated by the chip [31].

with a femtosecond laser and a PCA. The laser produces 100-fs optical pulses to generate electron-hole pairs with a short ( $\sim 1$ -ps) lifetime at the center of the PCA. These electron-hole pairs interact with

## Laser-Free Fully Electronic Samplers

### High-Speed Sampler

A silicon-based ultrawide-band sampler operating at hundreds of giga-samples per second would be an ideal receiver for pulse-based systems. However, many challenges must be overcome before such sampler is realized. One major challenge is the parasitic leakages in high-input frequencies; another is the poor efficiency of the gain stages in a terahertz regime.

To address the challenge of parasitic leakage from the input to the holding capacitor, a novel active cancellation technique is reported in [36]. A conventional sample-and-hold or track-and-hold architecture uses a transistor as a sampling switch. Ideally, this transistor should have very low impedance in the sample/track mode and very high impedance in the hold mode. However, in high-input frequencies, the isolation of the sampling transistor decreases rapidly. The parasitic  $C_{gs}$  and  $C_{gd}$  capacitances provide an additional path for the signal to leak to the holding capacitor. This leakage corrupts the voltage in the holding capacitor and reduces the performance of the sampler. In the active cancellation architecture introduced in [36] to mitigate the parasitic leakage, a dummy transistor is added in parallel to the sampling transistor. The dummy transistor is always in OFF mode and is fed with a signal that is complementary to the input signal. During the hold mode, the sampling transistor injects charge on the holding capacitor due to the parasitic leakage. At the same

time, the dummy transistor, fed with a negative copy of the input signal, injects a canceling charge on the holding capacitor. Because the charge injected by the dummy transistor is the negative of that injected by the sampling transistor, they cancel each other and mitigate the parasitic leakage. This is illustrated in Figure 12. Figure 13 shows that enabling the method of active cancellation can increase the isolation by  $> 30$  dB at 1 GHz. Figure 14 shows the micrograph of the chip that employs active cancellation during sampling. The chip was fabricated in a 45-nm CMOS–silicon-on-insulator (SOI) process and occupies an area of  $0.13 \text{ mm}^2$  [36].

To address the challenge of sampling tens of gigahertz of bandwidth, frequency-interleaved sampling architectures have been reported [37], [38]. Even though these

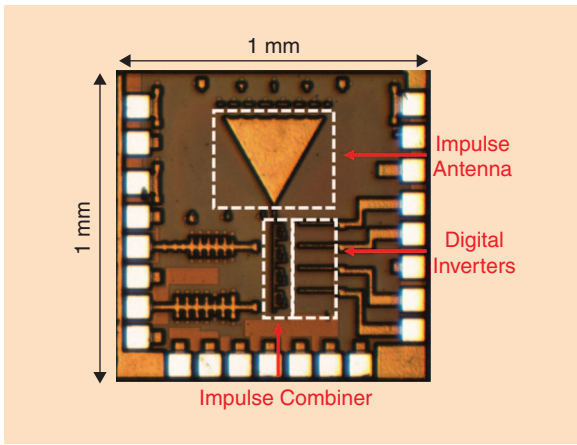


**Figure 10.** A micrograph of the chip for a 4-ps impulse radiator with pulse-amplitude modulation capability [31].

the electric field of the incoming wave to generate dc current. Because the lifetime of the electron–hole pairs is  $\sim 1$  ps, they can support a picosecond sampler. Although these systems have a large effective bandwidth (hundreds of gigahertz), the repetition rate of their femtosecond laser ( $< 100$  MHz) limits their sampling rate. Thus, the technique of sampling terahertz pulses with a femtosecond laser and a PCA is a sub-sampling method. Furthermore, these systems require an expensive laser, sensitive optical alignment, and a mechanical delay line to scan the sampling time with steps of smaller than 100 fs.

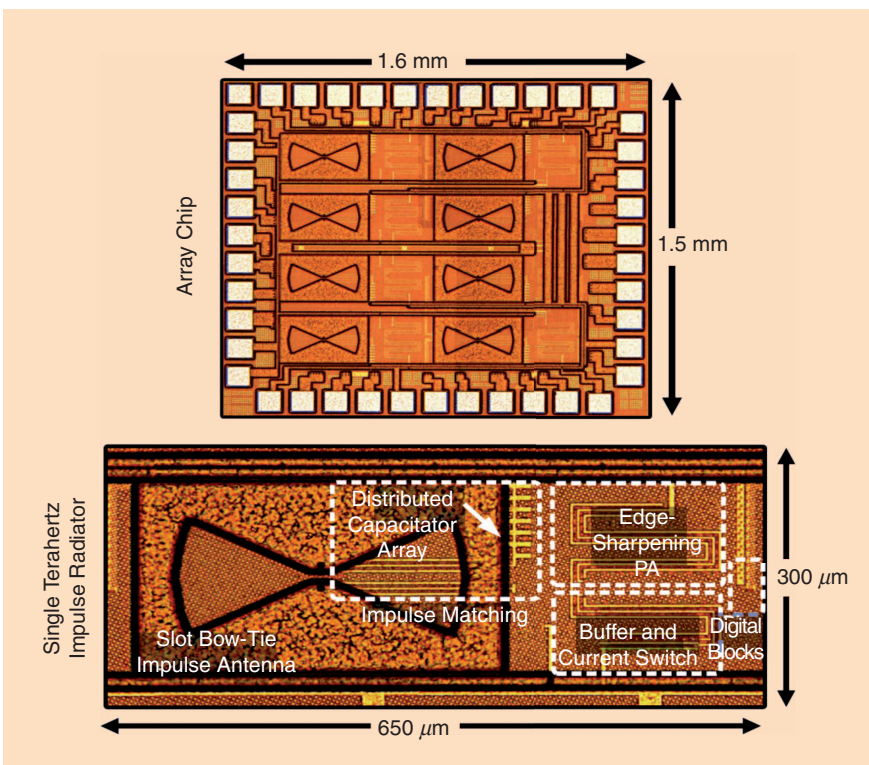


**Figure 11.** A micrograph of the chip for a 5.4-ps  $4 \times 2$  impulse radiating array in 90-nm SiGe BiCMOS [6].

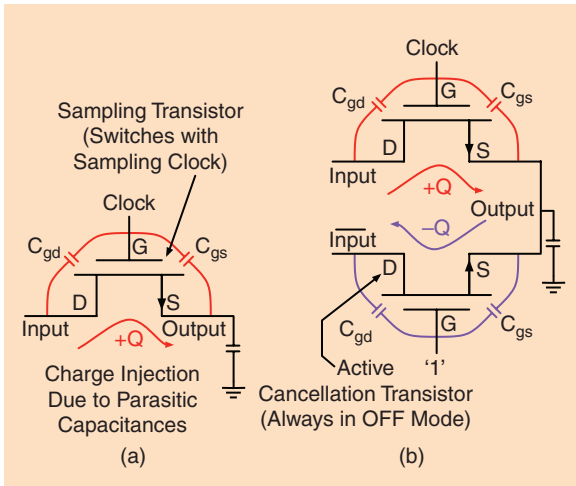


**Figure 12.** (a) A conventional sampling switch. Parasitic capacitances  $C_{gs}$  and  $C_{gd}$  provide an alternate path for the input signal to couple to the sampling capacitor. (b) A sampling switch with active cancellation. A dummy transistor, which is always off, is added in parallel to the sampling transistor. The parasitic charge dumped by the sampling switch is removed by the canceling transistor.

samplers are able to operate in a broader range of input frequencies, they suffer from a number of challenges, including aliasing, frequency spurs, and down-conversion frequency mismatch.

In many applications such as high-speed wireless communication and 3-D imaging radar, a picosecond receiver is required to measure the energy of the pulse. By measuring the energy of the picosecond pulse, it is possible to perform amplitude modulation and generate 200 Gb/s of information. For example, the 4-ps pulses reported in [31] can be interleaved in time by using multiple pulse radiators synchronized with each other. By applying 10-ps spacing between pulses and adding 2 b of amplitude modulation per pulse, it is possible to generate 200 Gb/s of information. Energy detectors recover both the energy of the pulse and its time of arrival. These two quantities are required to build a high-resolution 3-D imaging radar, as reported in the section “Experiments in 3-D Radar Imaging, Gas Spectroscopy, Secure Communication, and Precision Time Transfer.”

In addition to wireless communication and imaging radars, energy detectors can be used in time/frequency transfer links. In this application, picosecond pulses are radiated with a repetition

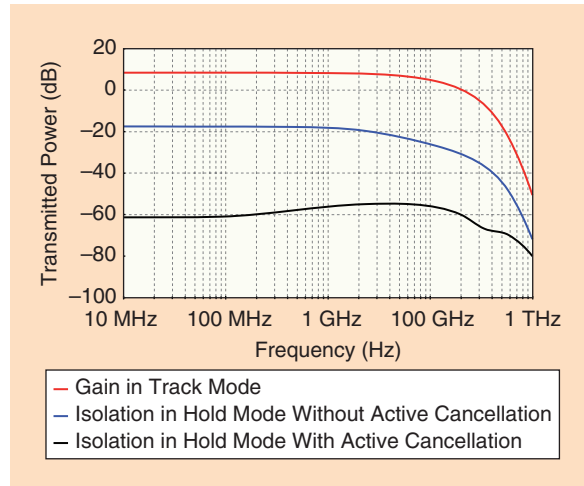


**Figure 13.** The simulated isolation between the track and hold modes, with and without the active cancellation block.

rate equal to the frequency of a clock that needs to be transferred. On the receiver part, an energy detector generates a clock signal by capturing the pulses and measuring their repetition rate. The following section explains how an energy detector based on self-mixing can be used to extract the repetition frequency of a picosecond impulse train.

### Self-Mixing Receiver

An impulse receiver based on a self-mixing technique was reported in [7]. The receiver detects picosecond impulses and extracts their repetition rate with a low timing jitter. Ultrashort pulses captured by the receiving antenna have a broadband frequency-comb spectrum, in which the center frequency is determined by the pulse-width. The repetition rate of these pulses sets the spacing between every two adjacent frequency tones. When the frequency comb is passed through a nonlinear block, different frequency tones mix with each other and produce the repetition tone at the output. A single bipolar

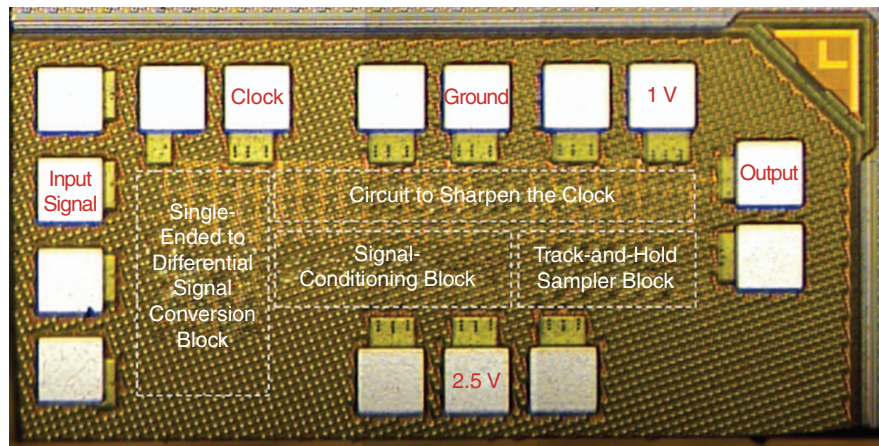


**Figure 14.** A micrograph of the chip for the track-and-hold amplifier in a 45-nm CMOS-SOI technology, measuring  $850 \mu\text{m} \times 450 \mu\text{m}$ , including pads [36].

## In a pulse-based imaging system, an array of radar transmitters fires pulses such that they arrive at a desired location in 3-D space at the same time.

transistor, biased at its most nonlinear region, is used as the mixer. The rest of the architecture includes an input amplifier chain at 50 GHz, a low-pass filter to remove the high-frequency feedthrough, and baseband amplifiers to amplify the main tone of the repetition rate with a tunable center frequency of 2–10 GHz. A broadband on-chip bow-tie antenna was also implemented to detect ultra-short pulses. The receiver was fabricated in a 130-nm SiGe BiCMOS process; a micrograph of the chip is shown in Figure 15.

### Experiments in 3-D Radar Imaging, Gas Spectroscopy, Secure Communication, and Precision Time Transfer

Here, we report on a few applications of pulse-based systems and demonstrate how the pulse sources/detectors can be used to produce high-resolution 3-D radar images, identify gas molecules based on their terahertz spectrum, establish a secure wireless communication, and transfer time with an accuracy of better than 100 fs.

#### 3-D Radar Imaging

In a pulse-based imaging system, an array of radar transmitters fires pulses such that they arrive at a desired location in 3-D space at the same time. When an object is in that location, the combined pulses produce a strong reflection. An array of pulse receivers

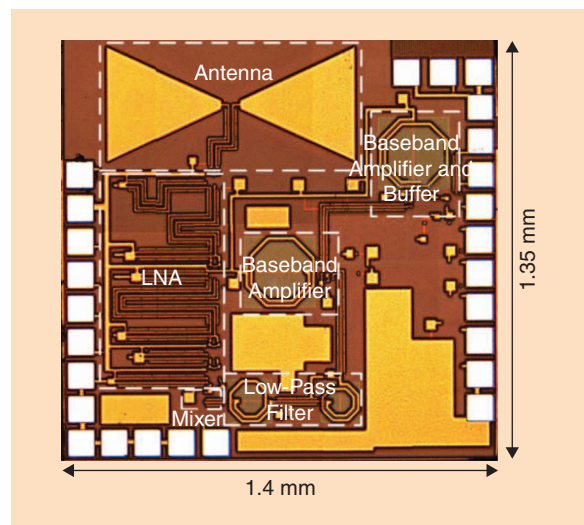


**Figure 15.** A micrograph of the chip for the fabricated impulse receiver [7]. LNA: low-noise amplifier.

synchronized with the transmitter array is used to detect these reflections and calculate the location of the object in a 3-D space.

To demonstrate this concept, a synthetic aperture is formed by a  $9 \times 9$  array. A single radiator is moved to 81 locations, and a sampling oscilloscope connected to a custom printed circuit board antenna is used to capture the impulses reflected from multiple objects. With a grid spacing of 5 mm, an effective aperture size of  $4 \text{ cm} \times 4 \text{ cm}$  is achieved. As shown in Figure 16, the whole imaging system consists of an impulse-radiating chip, a two-dimensional (2-D) travel stage, a custom-designed impulse-receiving antenna, and a sampling oscilloscope [26].

A four-step methodology is applied to perform 3-D imaging using a synthetic impulse-radiating array. As illustrated in Figure 17, the synthetic array is located on the XY plane.

#### Capturing Reflected Waveforms

A 2-D traveling stage moves the impulse radiator to construct a synthetic array. At the location of each element, the reflected waveforms from the targets are captured by the receiver antenna and then saved for further digital signal processing. After completing data acquisition at a fixed location, the 2-D traveling stage moves the impulse radiator to the location of the next element; then, the same data-acquisition operation is performed until a complete synthetic array is formed.

#### Beamforming Through Post-Processing at the Receiver

The impulses radiated from different elements in the synthetic array travel different distances to a certain point  $P(x, y, z)$  in the 3-D space. Therefore, the radiated impulses from all elements in the synthetic array can be aligned at point  $P$  when the appropriate time delays are added to the radiated impulses. Alternatively, these delays can be added at the receiver during post-processing. In our experiment, because a synthetic transmitter array is used, beamforming is done by post-processing the received waveforms [26].

#### Time-Domain Processing

Based on time-of-flight information, the received waveforms reflected from point  $P$  are filtered in time and saved. The image-pixel intensity of point  $P$  is chosen as the maximum amplitude of the saved waveform. As demonstrated in Figure 17(c), if there is no object at point  $P$ , the image-pixel intensity of point  $P$  is a negligible number (noise) because no reflection happens at point  $P$ . If there is an object at point  $P$ , the image-pixel intensity of point  $P$  becomes a large number proportional to the reflection coefficient of an object located in point  $P$ .

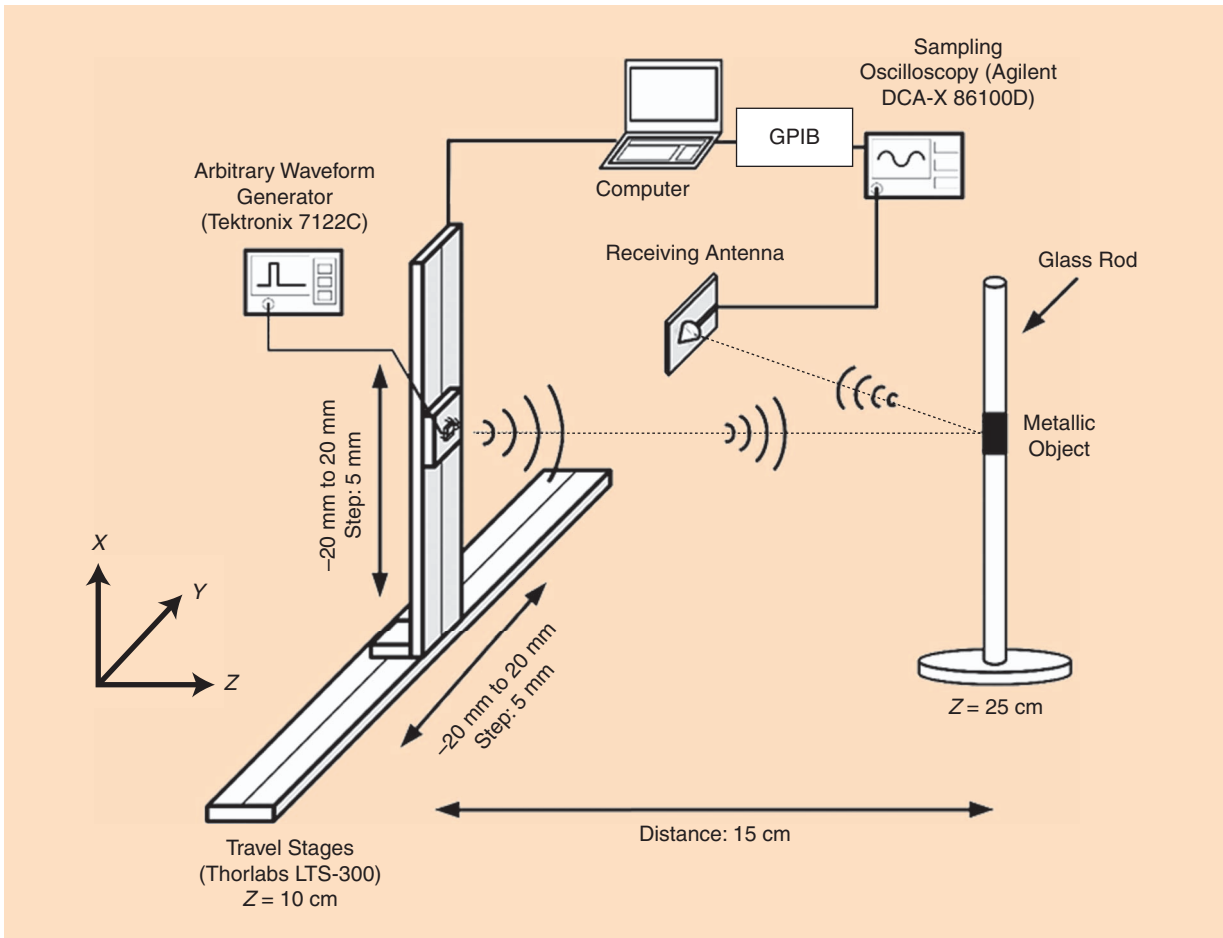


**Figure 16.** A custom-designed 3-D imaging setup. GPIB: general-purpose interface bus.

### Producing 3-D Images

As shown in Figure 17(d), a 2-D cross section can be generated by scanning point *P* on an image plane, which is defined as a finite XY plane with a fixed Z coordinate. The 3-D images are generated by varying the value of the Z coordinate of the image plane.

Several objects are used to demonstrate the capability of the 3-D imaging array. These objects include a small cylindrical aluminum foil, two spaced cylindrical aluminum foils, and a large ring covered by an aluminum foil. The chip in [26] emits 60-ps impulses with a repetition period of 3 ns. The objects are located at a distance of 15 cm ( $Z = 25$  cm) from the synthetic array. By post-processing the received waveforms from 81 locations, 3-D images are generated. As shown in Figure 18, at  $Z = 20$  cm, no object is detected. At  $Z = 25$  cm, which is the exact Z-coordinate of the objects, the produced mm-wave images show the object. Unlike prior work [39], [40], these high-resolution images are produced without using any lenses or reflectors.

### Gas Spectroscopy

Terahertz spectroscopy using frequency combs has become an effective technique for identifying gas

molecules [41], [42]. This technique can be used to detect the absorption lines in gasses caused by transitions between rotational states in the terahertz spectral range. In this experiment, a frequency comb is produced by a train of 5.4-ps impulses. Then, the repetition rate of the impulse train is varied to sweep the frequency tones and perform broadband terahertz gas spectroscopy [43]. Figure 19 illustrates a setup used for performing gas spectroscopy. In this experiment, a D2I chip as shown in Figure 11 radiates 5.4-ps impulses and a Virginia Diodes harmonic mixer (WR-1.5) coupled with a Keysight signal analyzer (N9030A) is used to receive the impulses. Figure 20 shows the absorption spectrum of ammonia gas with a 1% concentration in two different pressure levels. These results match with the expected absorption line of  $NH_3$  gas at 572 GHz.

### Pulse-Based Secure Communication

In conventional wireless communication systems, information is generated by a single transmitter at a single location in space. In this case, the information is broadcast in space, with directionality defined by the directivity of the transmitting antenna. A beamforming technique is used to concentrate power in a specific region; however, the information is still radiated

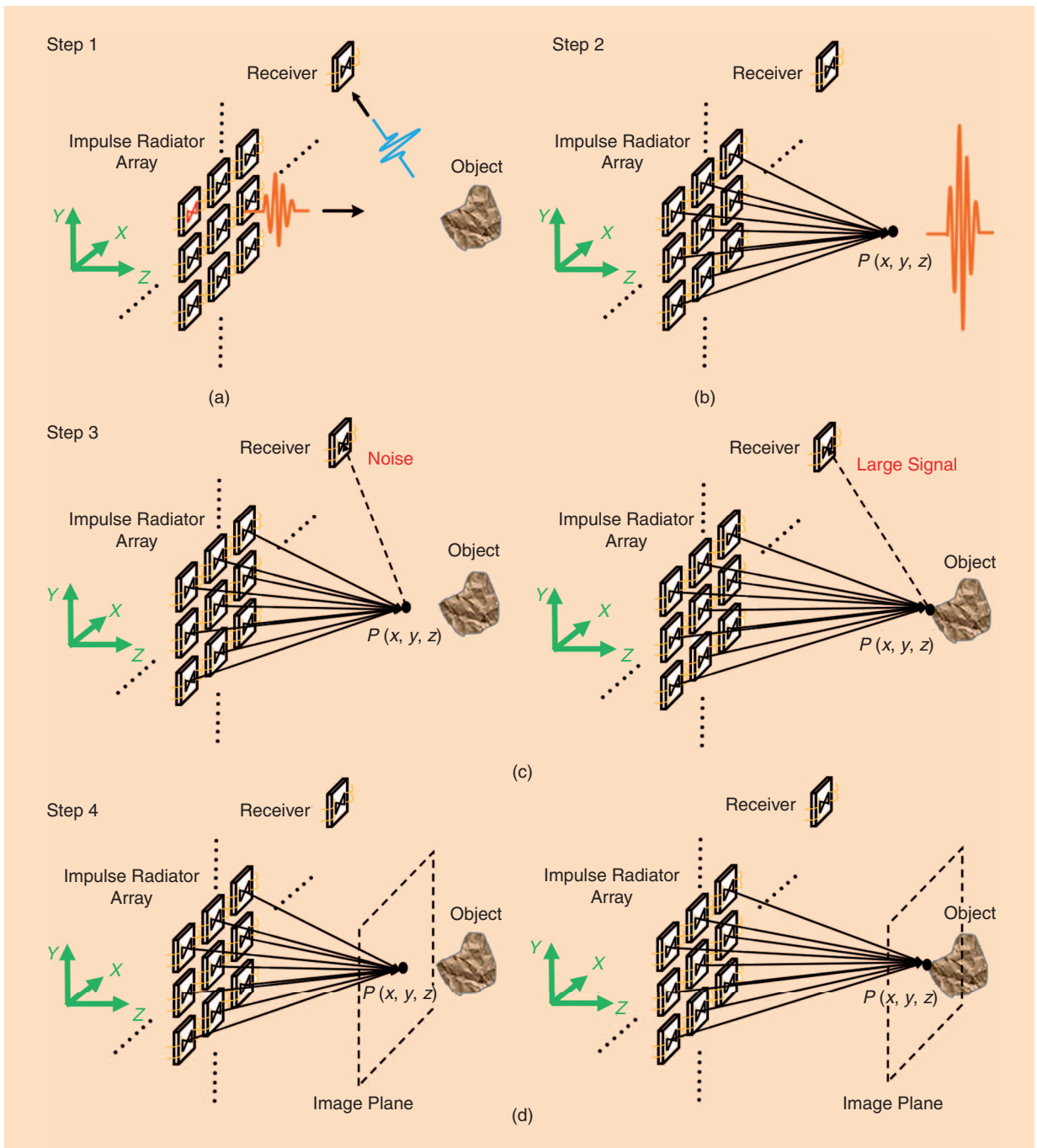


**Figure 17.** A 3-D imaging methodology: (a) capture of reflected waveforms, (b) digital beamforming through post-processing at the receiver, (c) time-domain processing, and (d) production of 3-D images.

everywhere in space. An eavesdropper equipped with a sensitive receiver looking at one of the side lobes of the radiation pattern can still receive signals and decode information. To secure the communication channel at the physical layer (e.g., an antenna level), the concept of near-field direct-antenna modulation or directional modulation was introduced [44]–[46]. In these schemes, the information was jointly generated and broadcast by different antennas, such that the time-domain signal integrity is preserved at the

direction of transmission. This prevents an eavesdropper from capturing the transmitted data outside an information beamwidth. In these schemes, instead of transmitting complete symbols from a single antenna, semi-symbols are transmitted from multiple antennas such that they combine to form a complete symbol at a specific direction in space. In other words, these schemes use joint spatial coding to produce correct symbols only at a desired direction in space. This concept is further explained in the next section.

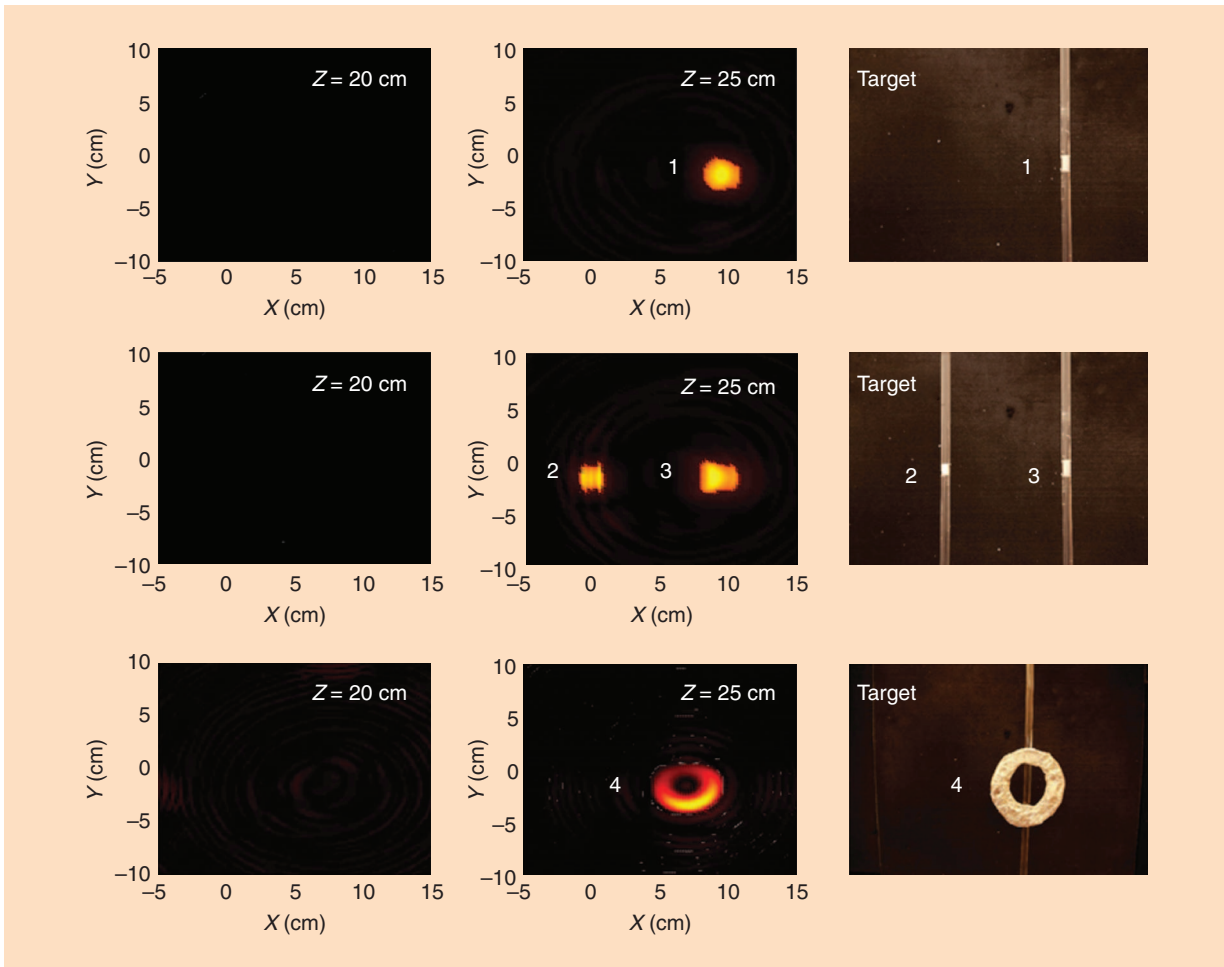


Figure 18. The captured 3-D images in three scenarios [26].

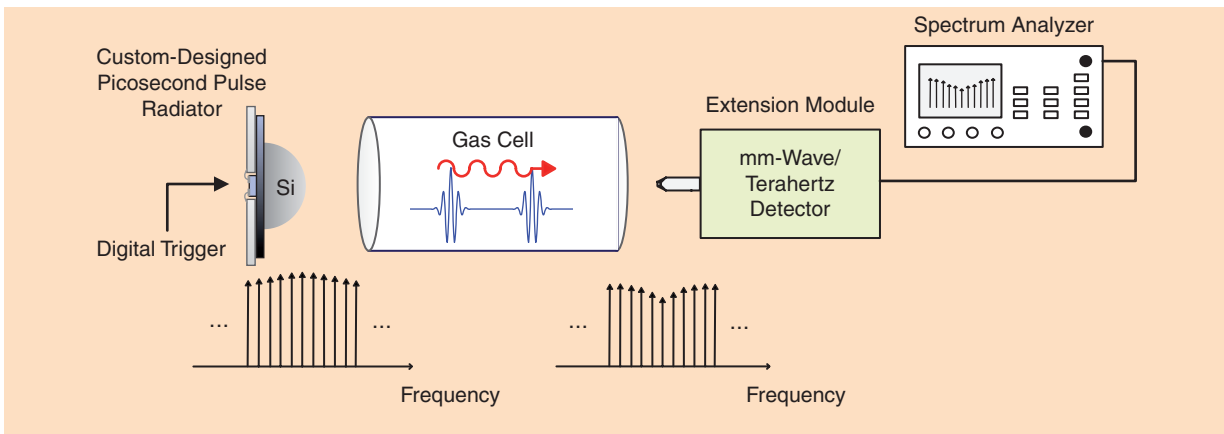


Figure 19. The terahertz gas spectroscopy setup [43]. Si: silicon.

### Joint Spatial Coding

In an architecture that uses joint spatial coding, multiple transmitting antennas are tightly synchronized at the symbol level to generate information at a single point (or direction) in space. A receiver present at this point receives the correct transmitted symbol and decodes the information. Receivers located at all other points in space receive corrupted symbols.

The concept of joint spatial coding is illustrated in Figure 21. Let the complete time-domain symbol be represented by  $s_{\text{orig}}(t)$ . This complete time-domain symbol can be divided into two semi-symbols,  $s_1(t)$  and  $s_2(t)$ , such that  $s_{\text{orig}}(t) = s_1(t) + s_2(t)$ . The signal  $s_1(t)$  is generated by the first transmitter  $\text{Tx}_1$ , and  $s_2(t)$  is generated by the second transmitter  $\text{Tx}_2$ . Let  $\tau_1$  and  $\tau_2$  be the propagation delays from  $\text{Tx}_1$  and  $\text{Tx}_2$  to a

# Picosecond generators and detectors enable 100+-Gb/s wireless communication, high-resolution 3-D imaging radars for security monitoring and autonomous driving, miniaturized radars for gesture detection and touchless smartphones, and spectrometers for explosive detection and gas sensing.

point  $P$  in space, respectively. The signal received at any point in space is given by  $s_1(t - \tau_1) + s_2(t - \tau_2)$ . A point  $P$  in space equidistant from these two transmitters will receive the transmitted signal at the same time and recover the original transmitted signal  $s_{orig}(t)$  after a delay. However, if point  $P$  is not equidistant from all the transmitters, their signals will arrive at different

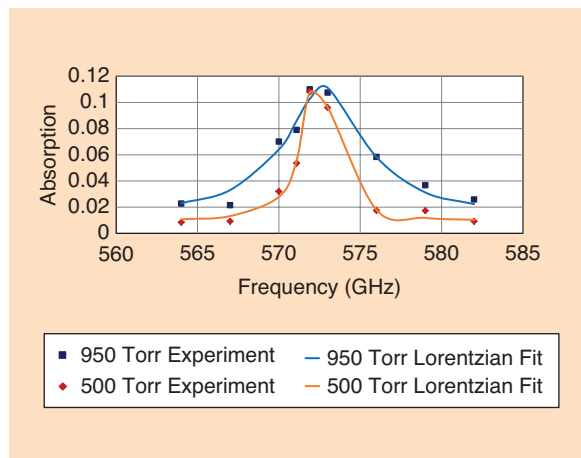


**Figure 20.** The measured absorption spectra for ammonia in two different pressures [43].

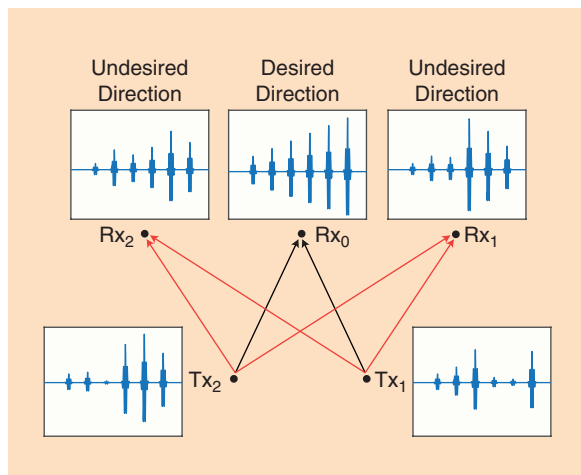


**Figure 21.** The pulse-based secure communication and concept of joint spatial coding.

times and produce a distorted time-domain waveform at point  $P$ .

Inspired by the aforementioned joint spatial coding, as shown in Figure 21,  $Tx_1$  and  $Tx_2$  transmit a ramp-modulated impulse train to a receiver that is equidistant from the transmitters. For a nonequidistant receiver, however, the received data are corrupted, which makes pulse-based communication spatially secure. In this application, the ability to produce shorter pulses reduces the information bandwidth and makes the channel more secure. In Figure 22, the error rate is plotted in an experiment where the distance of two transmitters is 120 cm and the duration of the radiated pulses is 200 ps. In this experiment, an information beamwidth of  $4^\circ$  is achieved [47].

## Precision Time Transfer and Localization

Traditionally, an energy detector is used to detect ultrashort pulses. Most energy detectors are diode-based and have several drawbacks. These detectors

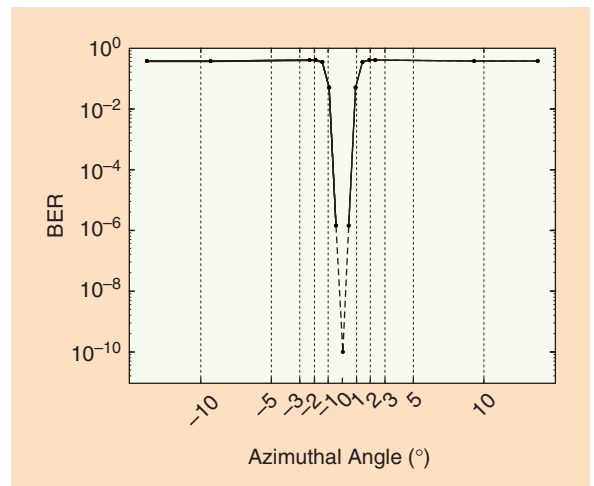


**Figure 22.** The bit-error rate (BER) versus angle [47].

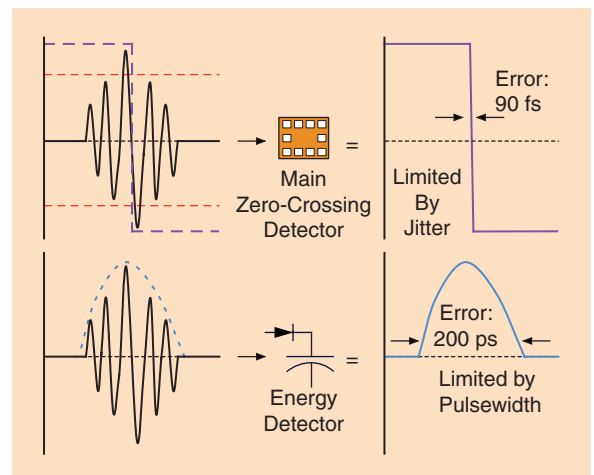


**Figure 23.** An energy detector versus a main zero-crossing detector [30].

detect the energy of the input signal irrespective of its shape or type, thus making them waveform nonselective. Moreover, in these detectors the timing accuracy is limited by the pulsewidth and not the pulse jitter, as illustrated in Figure 23. A waveform-selective, zero-crossing detector is reported that uses the main zero-crossing of the pulse to generate the timing signal [30]. In this architecture, the incoming signal is divided into three paths: the first path detects the rising edge of the pulse, the second path detects the falling edge of the pulse, and the third path detects all the zero-crossings. A high-speed AND-gate-equivalent circuitry is used to mask all the false zero-crossings from the main zero-crossing. This architecture is fabricated in a 130-nm SiGe BiCMOS process and used to detect 80 ps with a jitter of less than 100 fs. The chip was also used to measure the distance with an accuracy of 30  $\mu\text{m}$  [30]. Figure 24 shows the chip micrograph of the zero-detectors.

## Conclusions

The generation and detection of electromagnetic waves have evolved from Marconi's first spark-gap method to today's state-of-the-art solid-state picosecond pulse radiators. Picosecond generators and detectors enable wireless communication at 100+ Gb/s, high-resolution 3-D imaging radars for security monitoring and autonomous driving, miniaturized radars for gesture detection and touchless smartphones, spectrometers for explosive detection and gas sensing, precision time/frequency transfer, wireless synchronization of widely spaced arrays, and secure LOS communication. In this article, we reviewed some of these applications and reported silicon-based sources and detectors capable of generating and detecting picosecond pulses with high stability.

## Acknowledgments

The research reported in this article was partially funded by the National Science Foundation, the Keck Foundation, the Defense Advanced Research Projects Agency Microelectronics Technology Office, Semiconductor Research Corporation, and Texas Instruments.

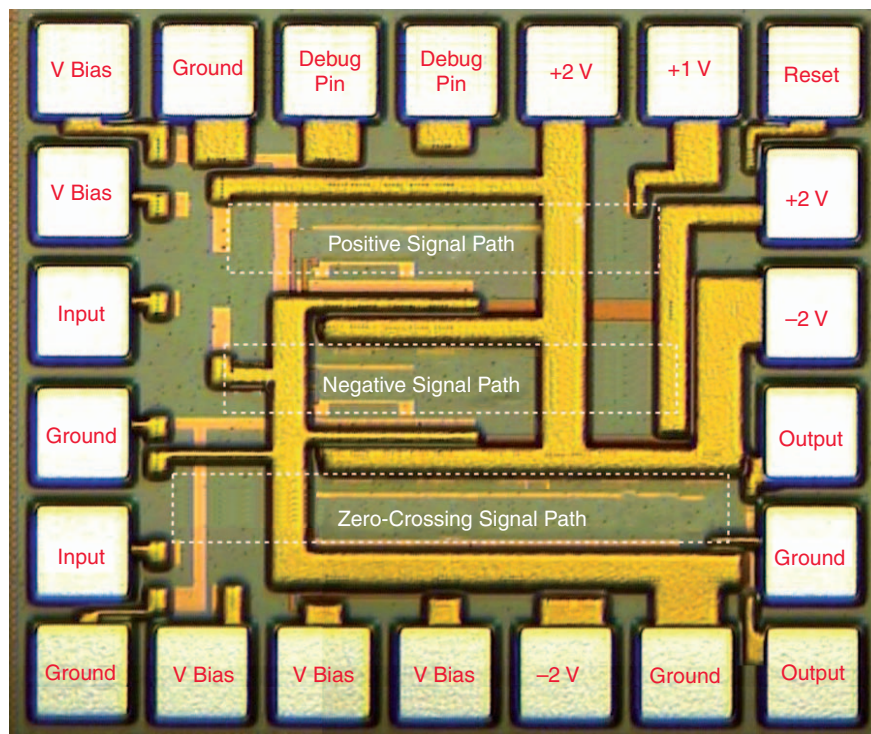


Figure 24. A micrograph of a chip with the zero-crossing detector [30].

## References

- [1] K. C. Huang and Z. Wang, "Terahertz terabit wireless communication," *IEEE Microwave Mag.*, vol. 12, no. 4, pp. 108–116, June 2011.
- [2] G. Fettweis and S. Alamouti, "5G: Personal mobile internet beyond what cellular did to telephony," *IEEE Commun. Mag.*, vol. 52, no. 2, pp. 140–145, Feb. 2014.
- [3] S. Bi, R. Zhang, Z. Ding, and S. Cui, "Wireless communications in the era of big data," *IEEE Commun. Mag.*, vol. 53, no. 10, pp. 190–199, Oct. 2015.
- [4] C. Dehos, J. L. Gonzalez, A. D. Domenico, D. Ktnas, and L. Dussopt, "Millimeter-wave access and backhauling: The solution to the exponential data traffic increase in 5G mobile communications systems?" *IEEE Commun. Mag.*, vol. 52, no. 9, pp. 88–95, Sept., 2014.
- [5] K. B. Cooper and G. Chattopadhyay, "Submillimeter-wave radar: Solid-state system design and applications," *IEEE Microwave Mag.*, vol. 15, no. 7, pp. 51–67, Nov.–Dec 2014.
- [6] M. M. Assefzadeh and A. Babakhani, "Broadband THz spectroscopic imaging based on a fully integrated  $4 \times 2$  digital-to-impulse radiating array with a full-spectrum of 0.03–1.03THz in silicon," in *Proc. IEEE Symp. VLSI Technology and Circuits*, 2016.
- [7] B. Jamali and A. Babakhani, "Sub-picosecond wireless synchronization based on a millimeter-wave impulse receiver with an on-chip antenna in 0.13  $\mu\text{m}$  SiGe BiCMOS," in *Proc. IEEE Microwave Theory and Technique Society Int. Microwave Symp.*, 2016, pp. 1–4.
- [8] M. Lazarus. (9 June 2016). What 5G engineers can learn from radio interferences troubled past [Online]. Available: <http://spectrum.ieee.org/telecom/wireless/what-5g-engineers-can-learn-from-radio-interferences-troubled-past>
- [9] D. McCormick. (10 Aug. 2015). See through walls by the glow of your Wi-Fi [Online]. Available: <http://spectrum.ieee.org/tech-talk/at-work/test-and-measurement/see-through-walls-by-the-glow-of-your-wifi>
- [10] L. J. Young. (6 Oct. 2015). Telecom experts plot a path to 5G [Online]. Available: <http://spectrum.ieee.org/telecom/wireless/telecom-experts-plot-a-path-to-5g>

- [11] R. Knipper, A. Brahm, E. Heinz, T. May, G. Notni, H. G. Meyer, A. Tnnermann, and J. Popp, "Thz absorption in fabric and its impact on body scanning for security application," *IEEE Trans. Terahertz Sci. Technol.*, vol. 5, no. 6, pp. 999–1004, Nov. 2015.
- [12] M. L. Psiaki and T. E. Humphreys. (29 Jul 2016). Protecting GPS from spoofers is critical to the future of navigation [Online]. Available: <http://spectrum.ieee.org/telecom/security/protecting-gps-from-spoofers-is-critical-to-the-future-of-navigation>
- [13] JPL BioSleeve enables precise robot control through hand and arm gestures. (16 May 2013). [Online]. Available: <http://spectrum.ieee.org/automaton/robotics/robotics-hardware/jpl-biosleeve-enables-precise-robot-control-through-hand-and-arm-gestures>
- [14] M. Lazarus. (22 Jan. 2015). Increasing use of radar tests spectrum authorities [Online]. Available: <http://spectrum.ieee.org/telecom/wireless/increasing-use-of-radar-tests-spectrum-authorities>.
- [15] E. Ackerman. (18 Aug. 2011). Gemini-scout will be the first one in to rescue trapped miners [Online]. Available: <http://spectrum.ieee.org/automaton/robotics/industrial-robots/geminiscout-will-be-the-first-one-in-to-rescue-trapped-miners>
- [16] E. Guizzo. (18 Oct. 2011). How Google's self-driving car works [Online]. Available: <http://spectrum.ieee.org/automaton/robotics/artificial-intelligence/how-google-self-driving-car-works>
- [17] T. Löffler, K. J. Siebert, N. Hasegawa, T. Hahn, and H. G. Roskos, "All-optoelectronic terahertz imaging systems and examples of their application," *Proc. IEEE*, vol. 95, no. 8, pp. 1576–1582, 2007.
- [18] A. V. Pipa and J. Ropcke, "Analysis of the mid-infrared spectrum of the exhaust gas from an atmospheric pressure plasma jet (appj) working with an argon–air mixture," *IEEE Trans. Plasma Sci.*, vol. 37, no. 6, pp. 1000–1003, June 2009.
- [19] S. Geng, D. Liu, Y. Li, H. Zhuo, W. Rhee, and Z. Wang, "A 13.3 mW 500 Mb/s IR-UWB transceiver with link margin enhancement technique for meter-range communications," *IEEE J. Solid-State Circuits*, vol. 50, no. 3, pp. 669–678, March 2015.
- [20] H. Hedayati and K. Entesari, "A 90-nm CMOS UWB impulse radio transmitter with 30-dB in-band notch at IEEE 802.11a System," *IEEE Trans. Microwave Theory Tech.*, vol. 61, no. 12, pp. 4220–4232, Dec. 2013.
- [21] S. Lee, S. Kong, C. Y. Kim, and S. Hong, "A low-power K-band CMOS UWB radar transceiver IC for short range detection," in *Proc. IEEE Radio Frequency Integrated Circuits Symp.*, 2012, pp. 503–506.
- [22] E. Ragonese, A. Scuderi, V. Giammello, E. Messina, and G. Palmisano, "A fully integrated 24 GHz UWB radar sensor for automotive applications," in *Proc. IEEE Int. Solid-State Circuits Conf. Tech. Dig.*, 2009, pp. 306–307, 307a.
- [23] S. Lee, C. Y. Kim, and S. Hong, "A K-Band CMOS UWB radar transmitter with a bi-phase modulating pulsed oscillator," *IEEE Trans. Microwave Theory Tech.*, vol. 60, no. 5, pp. 1405–1412, May 2012.
- [24] V. Jain, S. Sundararaman, and P. Heydari, "A 22-29-GHz UWB pulse-radar receiver front-end in 0.18- $\mu$ m CMOS," *IEEE Trans. Microwave Theory Tech.*, vol. 57, no. 8, pp. 1903–1914, Aug. 2009.
- [25] A. Arbabian, S. Callender, S. Kang, B. Afshar, J. C. Chien, and A. M. Niknejad, "A 90 GHz hybrid switching pulsed-transmitter for medical imaging," *IEEE J. Solid-State Circuits*, vol. 45, no. 12, pp. 2667–2681, Dec. 2010.
- [26] P. Chen and A. Babakhani, "A 30 GHz impulse radiator with on-chip antennas for high-resolution 3-D imaging," in *Proc. IEEE Radio and Wireless Symp.*, 2015, pp. 32–34.
- [27] A. Arbabian, S. Callender, S. Kang, M. Rangwala, and A. M. Niknejad, "A 94 GHz mm-wave-to-baseband pulsed-radar transceiver with applications in imaging and gesture recognition," *IEEE J. Solid-State Circuits*, vol. 48, no. 4, pp. 1055–1071, April 2013.
- [28] M. Assefzadeh and A. Babakhani, "A fully-integrated digitally-programmable  $4 \times 4$  picosecond digital-to-impulse radiating array in 65nm bulk CMOS," in *Proc. IEEE Microwave Theory Technique Society Int. Microwave Symp.*, 2016, pp. 1–4.
- [29] B. P. Ginsburg, S. M. Ramaswamy, V. Rentala, E. Seok, S. Sankaran, and B. Haroun, "A 160 GHz pulsed radar transceiver in 65 nm CMOS," *IEEE J. Solid-State Circuits*, vol. 49, no. 4, pp. 984–995, Apr. 2014.
- [30] H. Aggrawal and A. Babakhani, "An ultra-wideband impulse receiver for sub-100fsec time-transfer and sub-30  $\mu$ m localization," in *Proc. IEEE Radio and Wireless Symp.*, 2016, pp. 42–44.
- [31] P. Chen, Y. Wang, and A. Babakhani, "A 4ps amplitude reconfigurable impulse radiator with THz-TDS characterization method in 0.13 m SiGe BiCMOS," in *Proc. IEEE Microwave Theory Technique Society Int. Microwave Symp.*, 2016, pp. 1–4.
- [32] M. M. Assefzadeh and A. Babakhani, "Picosecond digital-to-impulse generator in Silicon," in *Proc. IEEE 16th Topical Meeting on Silicon Monolithic Integrated Circuits in RF Systems*, 2016, pp. 101–103.
- [33] M. Assefzadeh and A. Babakhani, "An 8-psec 13 dBm peak EIRP digital-to-impulse radiator with an on-chip slot bow-tie antenna in silicon," in *Proc. IEEE Microwave Theory Technique Society Int. Microwave Symp.*, 2014, pp. 1–4.
- [34] M. M. Assefzadeh and A. Babakhani, "A 9-psec differential lensless digital-to-impulse radiator with a programmable delay line in silicon," in *Proc. IEEE Radio Frequency Integrated Circuits Symp.*, 2014, pp. 307–310.
- [35] P. Chen, M. Hosseini, and A. Babakhani, "An integrated germanium-based optical waveguide coupled thz photoconductive antenna in silicon," in *Proc. Conf. Lasers and Electro-Optics, Optical Society of America*, 2016.
- [36] H. Aggrawal and A. Babakhani, "A 40GS/s track-and-hold amplifier with 62dB SFDR3 in 45 nm CMOS SOI," in *Proc. IEEE Microwave Theory Technique Society Int. Microwave Symp.*, 2014, pp. 1–3.
- [37] Q. Lei, Y. Zheng, and L. Siek, "Analysis and design of high performance frequency-interleaved ADC," in *Proc. IEEE Int. Symp. Circuits and Systems*, 2013, pp. 2022–2025.
- [38] L. Qiu, Y. J. Zheng, and L. Siek, "Design of frequency-interleaved ADC with mismatch compensation," *Electronics Lett.*, vol. 50, no. 9, pp. 659–661, Apr. 24 2014.
- [39] P. N. Chen, P. J. Peng, C. Kao, Y. L. Chen, and J. Lee, "A 94GHz 3-D-image radar engine with 4TX/4RX beamforming scan technique in 65 nm CMOS," in *Proc. IEEE Int. Solid-State Circuits Conf. Tech. Dig.*, vol. 50, no. 3, pp. 656–668, Mar. 2013.
- [40] A. Tang, G. Virbila, D. Murphy, F. Hsiao, Y. H. Wang, Q. J. Gu, Z. Xu, Y. Wu, M. Zhu, and M. C. F. Chang, "A 144 GHz 0.76 cm-resolution sub-carrier SAR phase radar for 3-D imaging in 65 nm CMOS," in *Proc. IEEE Int. Solid-State Circuits Conf.*, 2012.
- [41] Y. D. Hsieh, Y. Iyonaga, Y. Sakaguchi, S. Yokoyama, H. Inaba, K. Minoshima, F. Hindle, Y. Takahashi, M. Yoshimura, Y. Mori, T. Araki, and T. Yasui, "Terahertz comb spectroscopy traceable to microwave frequency standard," *IEEE Trans. Terahertz Sci. Technol.*, vol. 3, no. 3, pp. 322–330, May 2013.
- [42] A. S. Skryl, D. G. Pavelyev, M. Y. Tretyakov, and M. I. Bakunov, "High-resolution terahertz spectroscopy with a single tunable frequency comb," *Opt. Express*, 2014.
- [43] M. Assefzadeh, B. Jamali, A. Gluszek, A. Hudzikowski, J. Wojtas, F. Tittel, and A. Babakhani, "Terahertz trace gas spectroscopy based on a fully-electronic frequency-comb radiating array in silicon," in *Proc. Conf. Lasers and Electro-Optics*, 2016.
- [44] A. Babakhani, D. B. Rutledge, and A. Hajimiri, "Transmitter architectures based on near-field direct antenna modulation," *IEEE J. Solid-State Circuits*, vol. 43, no. 12, pp. 2674–2692, Dec. 2008.
- [45] J. Lavaei, A. Babakhani, A. Hajimiri, and J. C. Doyle, "A study of near-field direct antenna modulation systems using convex optimization," in *Proc. American Control Conf.*, 2010, pp. 1065–1072.
- [46] A. Babakhani, D. B. Rutledge, and A. Hajimiri, "Near-field direct antenna modulation," *IEEE Microwave Mag.*, vol. 10, no. 1, pp. 36–46, Feb. 2009.
- [47] H. Aggrawal, R. Puhl, and A. Babakhani, "Ultra-wideband pulse-based directional modulation," in *Proc. IEEE Microwave Theory and Technique Society Int. Microwave and Radio Frequency Conf.*, 2015.

